## PAPER

Check for updates

# Optimizing hole transport efficiency in perovskite solar cells by structural modeling of 1,4-dihydropyrrolo[3,2-*b*]pyrroles with various donors: a DFT approach

Iqra Shafiq, [ID] [a] Fatima Sarwar,[a] Abid Hussain,[a] Khalid Mahmood, [ID] *[b] Muhammad Imran [ID] [cd] and Ke Chen*[e]

Hole transport materials (HTMs) are crucial in controlling charge dynamics in perovskite solar cells (PSCs), notably in processes such as interfacial charge separation and electron recombination. Currently, a series of 1,4-dihydropyrrolo[3,2-*b*]pyrrole (DHPP) based HTMs (**PSR** and **PSD1–PSD7**) possessing a D−π−D architecture was designed through molecular engineering with various heterocyclic donors. The photovoltaic and optoelectronic characteristics of the designed derivatives were investigated using the M06 functional with the 6-311G (d,p) basis set in DFT/TD-DFT approaches. All compounds displayed energy gaps in the range of 3.113–3.678 eV, with absorption spectra in the range of 420.5 to 444.3 nm. Frontier molecular orbital (FMO) investigations demonstrated an efficient intramolecular charge transfer (ICT) from the DHPP core to terminal donors. The significant charge transfer was further supported by the transition density matrix maps and the density of states. All designed chromophores revealed lower exciton binding energy values ($E_b$ = 0.310–0.772 eV), showing higher exciton dissociation rates with enhanced charge transfer. A benchmark analysis with spiro-OMeTAD used as a standard in HTM studies demonstrated that the engineered chromophores exhibited good hole transport performance. These results indicate that structural modeling of organic chromophores with heterocyclic donors can effectively tune their photovoltaic properties, making them promising candidates for use as efficient HTMs.

*[a]Institute of Chemistry, Khwaja Fareed University of Engineering & Information Technology, Rahim Yar Khan, 64200, Pakistan*

*[b]Institute of Chemical Sciences, Bahauddin Zakariya University, Pakistan. E-mail: khalidmahmood@bzu.edu.pk; kmchemist@yahoo.com*

*[c]Department of Chemistry, Faculty of Science, King Khalid University, P.O. Box 9004, Abha 61413, Saudi Arabia*

*[d]Research Center for Advanced Materials Science (RCAMS), King Khalid University, P. O. Box 9004, Abha 61514, Saudi Arabia*

*[e]Department of Infectious Diseases, The Affiliated Hospital of Southwest Medical University, Luzhou 646000, China. E-mail: chen_ke@swmu.edu.cn*

## Introduction

Photovoltaic (PV) technology, which converts solar energy into electricity, is believed to be one of the most effective techniques to solve the growing worldwide energy crisis.[1] Among various PV technologies, perovskite solar cells (PSCs) have gained remarkable attention owing to their excellent optoelectronic properties, such as strong light absorption, long carrier diffusion lengths, defect tolerance, and tunable band gaps.[2] Recent advances have enabled PSCs to achieve power conversion efficiencies (PCEs) exceeding 25%, comparable to traditional silicon-based solar cells, while offering the advantage of low-temperature and solution-based fabrication.[3,4] Recently,

hybrid organic-inorganic PSCs have become a promising photovoltaic (PV) candidate[5] because of their pleasing optical and electrical properties for PV devices, including suitable and strong optical absorption, extended carrier diffusion lengths, elevated defect tolerance, and tunable energy gaps.[6] A critical component of PSCs is the hole transport material (HTM), which governs charge extraction, transport, and recombination dynamics at the perovskite interface.[7] The most widely used HTM, 2,2′,7,7′-tetrakis(*N,N*-di-*p*-methoxyphenylamine)-9,9′-spirobifluorene (spiro-OMeTAD), provides excellent performance but suffers from high costs, low intrinsic hole mobility, and complex synthesis, hindering its large-scale deployment.[8] An efficient HTM should possess high chemical stability, smooth morphology, appropriate energy level alignment with the perovskite layer, high transparency, and strong hole mobility to minimize recombination losses. These requirements have driven extensive research on cost-effective and tunable organic semiconductors, which can be precisely engineered through molecular design strategies.[8,9] Both positive charge transfer processes and unfavorable recombination[9,10] processes greatly impact power conversion efficiency (PCE).[11] In this context, HTMs should (i) be physically and chemically stable, (ii) have a compact structure, (iii) exhibit exceptional

uniformity and low surface roughness for consistent fabrication, (iv) maintain high transparency, (v) have perfect energy levels (HOMO and LUMO) relative to the perovskite layers to allow hole transmission while preventing electron recombination at the interfaces, and (vi) have a low defect density to reduce charge recombination inside the HTMs.[12,13] The pursuit of cost-effective and scalable HTMs has intensified, leading to exploration in various categories: (i) inorganic materials like nickel oxide and copper thiocyanate, which are affordable and have facile synthesis but face challenges such as interfacial recombination losses and processing constraints; (ii) carbon-based materials, including carbon and graphene nanotubes, known for their excellent conductivity and potential for large-scale production; and (iii) organic semiconductors, which can be tailored to meet specific application needs, provided their molecular structure remains stable under environmental influences.[14–19] Two-dimensional conjugated frameworks with extended chemical delocalization across fused aromatic units are often favored over many alternatives because the π-conjugated regions are uniformly distributed, enhancing the intrinsic structure.[14,20] The literature is saturated with various examples in which the organic molecule comprises a donor core as a central unit, such as carbazole, triphenylamine (TPA), benzothiophene-based frameworks,[21] naphthalene diamine (NDI) and indacenodithiophene (IDT), displaying good photovoltaic characteristics as HTMs.[20] 1,4-Dihydropyrrolo[3,2-*b*]pyrroles (DHPPs) are the least studied diheteropentalenes, which are a type of 10-π-electron heterocycle. Comparably, thieno[3,2-*b*]thiophene and thieno[3,2-*b*]pyrrole cores are well-established, extensively researched, and widely employed in several fields of study. Their electrical configurations render them intriguing from both theoretical and synthetic viewpoints. Literature studies have revealed that they have attracted significant attention in areas such as optoelectronics, polymers
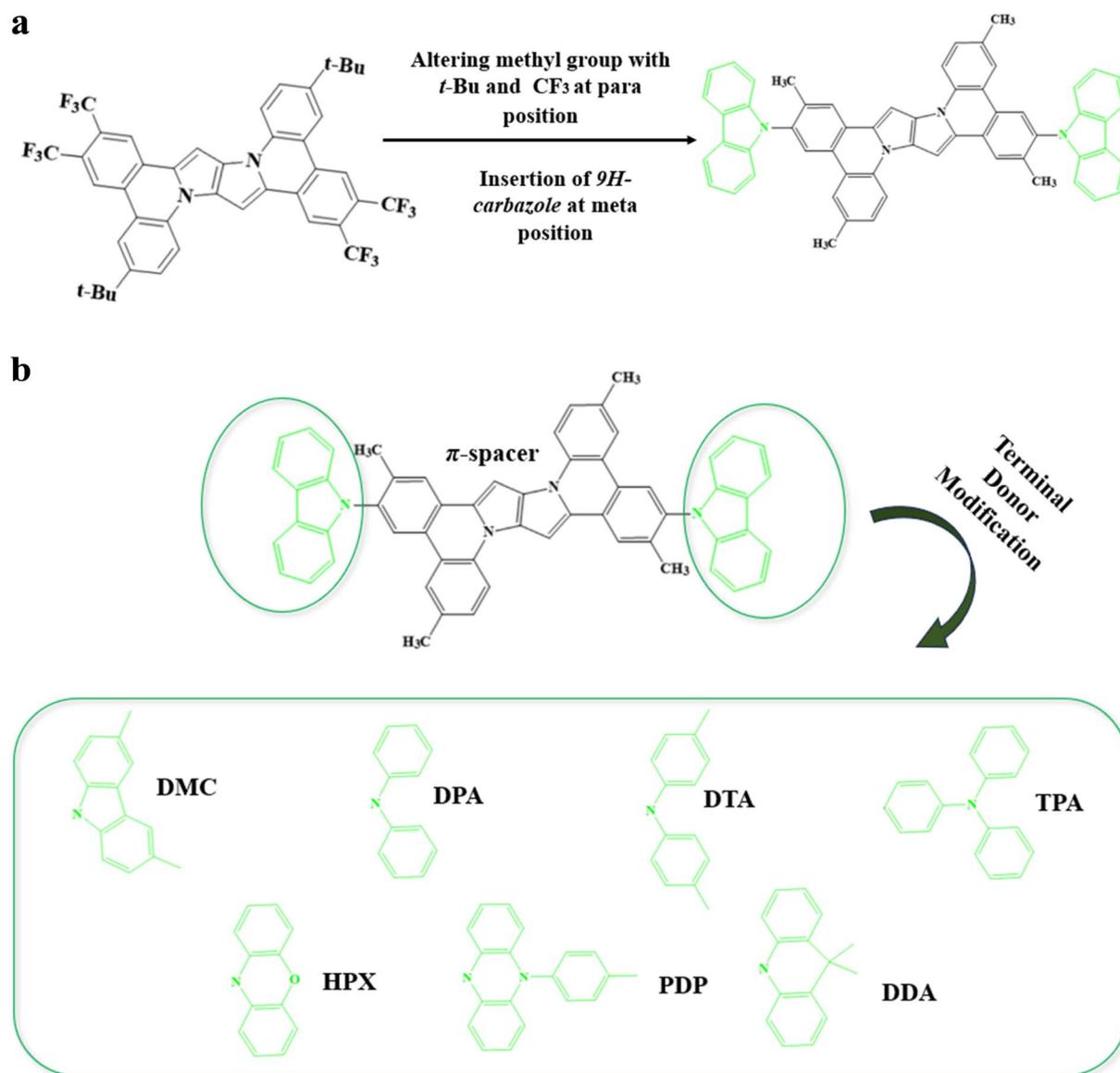


Fig. 1  (a) Altering **TAPAA** into **PSR** by inserting methyl and donor groups. (b) Depiction of terminally modified donor units.

for organic light-emitting diodes (OLEDs), and various photovoltaic applications.[22] Their planar configuration facilitates efficient π–π stacking, promoting improved charge mobility in photovoltaic devices. Additionally, the conjugated system in dihydropyrrole supports effective electron delocalization, essential for light absorption and efficient charge separation. Furthermore, dihydropyrrole derivatives can be readily functionalized, allowing precise tuning of energy levels and enhancing their compatibility with other solar cell components.[23]

By considering the aforementioned qualities of DHPP-based chromophores, recently, a series of different-donor chromophores (**PSD1–PSD7**) with a D–π–D configuration was designed for use as HTMs in PSCs. To the best of our knowledge, the application of DHPP-based systems in PSCs has not been reported previously. Following their structural confirmation, the photovoltaic capabilities of **PSD1–PSD7** were studied by DFT/TD-DFT methodologies. The insights obtained from this work are expected to guide the development of stable, low-cost, and high-performance DHPP-based HTMs for next-generation perovskite solar cells.

### Computational procedure

The Gaussian 16 (ref. 24) software was utilized to conduct all quantum chemical calculations in the current study. The M06 (ref. 26) functional with the 6-311G(d,p) (ref. 30) basis set was utilized to investigate the electrical and optical properties of the designed compounds. First, geometrical optimization was performed in order to obtain the true minima geometries. Then, these geometries were further utilized to perform other analyses for investigating the optoelectronic characteristics. Graphical representations, including the DOSs, absorption spectra, and TDMs, were developed using PyMOlyze,[25] Origin 8.5 (ref. 26) and Multiwfn 3.7,[27] respectively. The FMO results were interpreted *via* Avogadro[28] software utilizing Gaussian outputs. Further, GaussSum[29] Version 2.0 was applied to regain the UV-vis data from the output files. Chemical reactivity characteristics such as ionization potential (IP),[30] electron affinity (EA),[31] electronegativity (X),[32] chemical potential (μ),[41] electrophilicity index (ω),[33] softness (σ),[34] and hardness (η)[35] were determined *via* eqn (1)–(7), respectively.

## Results and discussion

The current study focuses on the computational investigation of photovoltaic characteristics of DHPP-based molecules. In the present investigation, **PSR** is used as a reference developed from an a synthesized parent molecule **TAPP** (1,2,4,5-tetraaryl-1,4-dihydropyrrolo[3,2-*b*]pyrrole)[36] by altering the *t*-butyl groups with methyl groups and replacement of –CF₃ group with donor 9-*H*-carbazole (HCZ) at *meta* position, as displayed in Fig. 1a. Mechanistically, the increased conjugation and planarity lowers the HOMO–LUMO gap, which increase the red-shifted absorption in such compound. The more delocalized hole density and reduced reorganization energy expected for such a rigid, fused scaffold is favorable for hole transport and extraction when

used as an HTM. Prior studies have shown that **TAPP** derivatives are readily functionalized for self-assembly and film formation and that porphyrin fusion strategies lead to extended absorption and improved optoelectronic behavior.[37]

Hence the configuration of **PSR** changed into a D–π–D by inserting an effective donor (D) unit. Moreover, other D groups, such as, 3,6-dimethyl-9-*H*-carbazole (DMC), diphenylamine (DPA), di-*p*-tolylamine (DTA), triphenylamine (TPA), 10-*H*-phenoxazine (HPX), 5-(*p*-tolyl)-5,10-dihydrophenazine (PDP) and 9,9-dimethyl-9,10-dihydroacridine (DDA), are attached with **DHPP** core and designed **PSD1–PSD7** chromophores (Fig. 1b). The optimize molecular structures of all the designed compounds are depicted in Fig. 2 and their chemical structures are shown in Fig. S1. Cartesian coordinates are provided in Tables S1–S8. The primary goal of this research is to evaluate the HTM performance of the designed compounds and explore their promising attributes in optoelectronics by systematically changing the donor groups while maintaining an unchanged core structure. To achieve this, we conducted a computational analysis using DFT/TD-DFT methods, specifically the M06/6-311G(d,p) functional, and examined the following properties: (i) energy gaps (ΔE), (ii) maximum absorption wavelengths (λ_max), (iii) global reactivity descriptors, (v) transition density matrices (TDMs), (vi) binding energies (E_b), and (vii) hole–electron investigations. Following the computational calculations, density of states (DOS) analysis was carried out using DFT, while frontier molecular orbitals (FMOs), UV-visible spectra, and transition density matrices (TDM) were analyzed through the TD-DFT approach to investigate their photovoltaic characteristics.
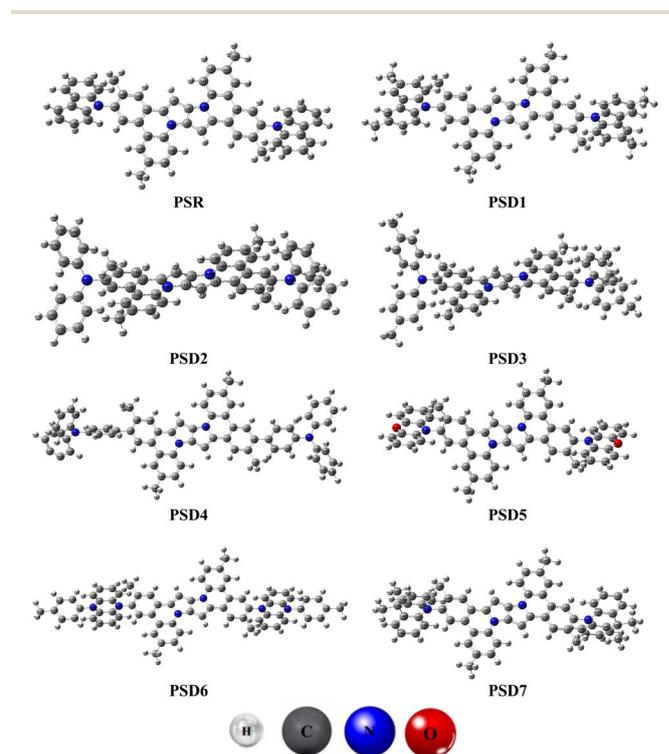


Fig. 2 Optimized geometries of **PSR** and **PSD1–PSD7**.

### Frontier molecular orbitals (FMOs)

Frontier molecular orbitals (FMOs) consist of two main orbitals: highest occupied molecular orbital (HOMO) and lowest unoccupied molecular orbital (LUMO).[38] The FMOs are useful for describing the affinity and interaction of the created molecule with other moieties.[39] It also assist us in identifying the reactive regions inside any $\pi$-electron systems.[40,41] The energy gap ($E_{gap} = E_{LUMO} - E_{HOMO}$) illustrates the electron transfer properties, reactivity, softness, and hardness of the molecule.[42] Moreover, the $E_{gap}$ is regarded as an essential parameter for assessing the photovoltaic qualities. The HOMO corresponds to the orbitals having an electron-giving propensity, whereas the LUMO corresponds to the orbitals having an electron-accepting tendency.[43] A literature study shows that smaller the energy gap, greater will be the charge transfer and *vice versa*.[44] The FMO analysis of **PSR** and **PSD1–PSD7** is performed, and the results are listed in Table 1, whereas HOMO−1, LUMO+1, HOMO−2 and LUMO+2 displays in Tables S9 and Fig. S2.

The HOMO/LUMO energy values of **PSR–PSD7** are determined to be −5.346/−1.685, −5.331/−1.666, 5.100/−1.553, −5.029/−1.573, −5.127/−2.014, −5.349/−1.685, −4.901/−1.621 and 5.311/−1.633 eV, correspondingly. The terminal donor in **PSR** was substituted with several potent thiophene rings of the $\pi$-linker. However, a drop in the energy gap is visible among all the designed derivatives, as illustrated in Table 1. The increase in HOMO energy arises because the electron-donating group introduces a higher energy $\pi$-orbital that mixes with the conjugated system, raising the HOMO level. This enhanced delocalization facilitates intramolecular charge transfer from donor to acceptor units, thereby narrowing the energy gap.[45] The calculated energy gap values between the HOMO and LUMO of **PSR–PSD7** are 3.661, 3.665, 3.547, 3.516, 3.113, 3.664, 3.280, and 3.678 eV, respectively. Among all the designed compounds, **PSD4** exhibits the smallest energy gap of 3.113 eV, which can be attributed to the connected donor TPA. The nitrogen core of TPA enhances electron delocalization throughout the phenyl rings, thereby improving conjugation and stabilizing the HOMO energy level at an elevated state.[46] Similarly, **PSD7** with the greatest energy gap of 3.678 eV is ascribed to the influence of donor DDA containing two methyl groups, which inhibit delocalization and conjugation, which leads to greater energy gap between the HOMO and LUMO.

Moreover, **PSR**, **PSD1**, **PSD2**, **PSD3**, **PSD5**, and **PSD6** display a narrower energy gap than **PSD7** owing to the existence of HCZ, DMC, DPA, DTA, HPX and PDP donors that would likely boost the inductive and resonance effects. Overall, all the proposed chromophores exhibit the following ascending order of orbital energy gaps: **PSD4** < **PSD6** < **PSD3** < **PSD2** < **PSDR** < **PSD5** < **PSD1** < **PSD7**. The calculated frontier molecular orbital energies of the **PSD** series (**PSR** and **PSD1–PSD7**) were compared with the well-known hole transport material spiro-OMeTAD to evaluate their
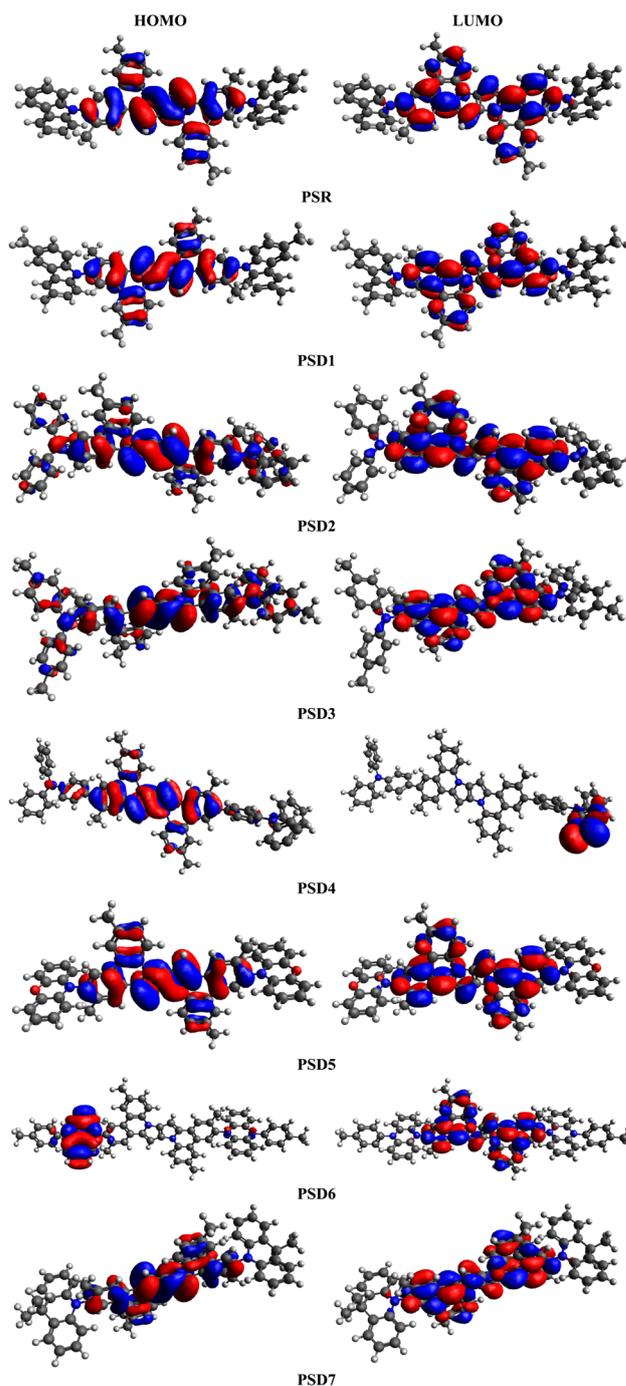


**Fig. 3** HOMOs and LUMOs of the studied compounds (PSR and PSD1–PSD7).

**Table 1** $E_{HOMO}$, $E_{LUMO}$ and energy gap ($\Delta E$) for PSR and PSD1–PSD7 in eV[a]

| Compounds | $E_{HOMO}$ | $E_{LUMO}$ | $E_{gap}$ |
|---|---|---|---|
| **PSR** | −5.346 | −1.685 | 3.661 |
| **PSD1** | −5.331 | −1.666 | 3.665 |
| **PSD2** | −5.100 | −1.553 | 3.547 |
| **PSD3** | −5.029 | −1.573 | 3.516 |
| **PSD4** | −5.127 | −2.014 | 3.113 |
| **PSD5** | −5.349 | −1.685 | 3.664 |
| **PSD6** | −4.901 | −1.621 | 3.280 |
| **PSD7** | −5.311 | −1.633 | 3.678 |

[a] Band gap = $E_{LUMO} - E_{HOMO}$, units in eV.

potential for use in perovskite solar cells. The HOMO levels of the PSDs (−4.90 to −5.35 eV) are comparable to that of spiro-OMeTAD ($\approx$ −5.0 to −5.2 eV), which facilitates efficient hole extraction from the perovskite valence band.[47] Their relatively high LUMO energies (−1.55 to −2.01 eV) indicate strong electron-blocking ability, thus reducing interfacial recombination.[48] Moreover, their large band gaps (3.11–3.68 eV) suggest good optical transparency, favorable for maximizing light absorption in PSCs. These findings identify **PSD4** and **PSD6** as promising candidates for efficient and stable hole transport materials.

The surface illustrations of the FMOs improve the understanding of the charge transfer phenomena reported in **PSR** and **PSD1–PSD7**. In the HOMO, the electronic density is primarily concentrated on the π-spacer, with minimal presence in the donor component. Conversely, in the LUMO, the charge density increases in the π-spacer while decreasing in the donor moieties, as illustrated in Fig. 3. The integration of effective donor groups with strong electron-donating units results in a reduced $E_{\text{gap}}$, enhancing efficient charge transfer from the π-spacer to the end-capped donor regions, thereby rendering them effective HTMs.

### Global reactivity descriptors (GRD)

The strength of FMOs ($E_{\text{gap}} = E_{\text{LUMO}} - E_{\text{HOMO}}$) is important to identify global reactivity descriptors, such as the ionization potential (IP), chemical hardness ($\eta$), global electrophilicity index ($\omega$), chemical softness ($\sigma$), electron affinity (EA), chemical potential ($\mu$), and electronegativity ($X$).[32,49–51] The IP and EA are determined *via* eqn (1) and (2), respectively.[52] The global descriptors ($\eta$, $\mu$, $X$, $\sigma$, and $\omega$) are determined utilizing the Koopmans' theorem *via* the eqn (3)–(7).[53]

$$\text{IP} = -E_{\text{HOMO}} \tag{1}$$

$$\text{EA} = -E_{\text{LUMO}} \tag{2}$$

$$X = \frac{[\text{IP} + \text{EA}]}{2} \tag{3}$$

$$\eta = \frac{[\text{IP} - \text{EA}]}{2} \tag{4}$$

$$\mu = \frac{E_{\text{HOMO}} + E_{\text{LUMO}}}{2} \tag{5}$$

$$\sigma = \frac{1}{2\eta} \tag{6}$$

$$\omega = \frac{\mu^2}{2\eta} \tag{7}$$

The ionization potential (IP) reflects the capability of a molecule to accept or donate electrons and corresponds to the energy required to withdraw an electron from the HOMO. Chemical potential, energy gap, hardness, and compound stability are directly correlated, while reactivity is inversely related to these properties. Consequently, a molecule with a larger energy gap is considered harder, less reactive, and more kinetically stable. Additionally, the electronegativity of the substituents influences molecular stabilization and determines a compound's ability to attract electrons.[52] Whereas, EA illustrates the electron-accepting ability of a molecule.[54] All designed compounds display discrete trends in theoretically computed EA values.

The electron-accepting and electron-donating characteristics of **PSR** and **PSD1–PSD2** can be evaluated using their ionization potential (IP) and electron affinity (EA) values. As shown in Table 2, the ionization potential of the developed compounds is lower than that of **PSR** (5.346 eV), except for **PSD5** (5.349 eV), due to presence of the **HPX** donor having electronegative atoms (N and O) and structural conjugation. This shows a simple electron elimination procedure with a lesser energy required in the proposed derivatives as compared to the **PSR**. The computed descendant order of IP values is: **PSD5** > (5.349) > **PSR** (5.346) > **PSD1** (5.331) > **PSD7** (5.311) > **PSD4** (5.127) > **PSD2** (5.100) > **PSD3** (5.029 eV). Similarly, **PSD4** demonstrates the greatest EA among all the corresponding derivatives. This change can be due to the specific **TPA** donor having conjugating phenyl rings and nitrogen electronegativity, results in a large rise in the EA. The IP acts as a helpful component for illuminating the capability of electrons to stray from an equilibrium condition.[41] It displays the decreasing order for studied molecules is as follows: **PSD4** (−3.570) > **PSD5** (−3.517) > **PSR** (−3.515) > **PSD1** (−3.498) > **PSD7** (−3.472) > **PSD2** (−3.326) > **PSD3** (−3.271) >

**Table 2** Global reactivity parameters of studied compounds (**PSR** and **PSD1–PSD7**)[a]

| Compounds | IP | EA | $X$ | $\eta$ | $\mu$ | $\omega$ | $\sigma$ | $\Delta N_{\text{max}}$ |
|---|---|---|---|---|---|---|---|---|
| **PSR** | 5.346 | 1.685 | 3.515 | 1.830 | −3.515 | 3.375 | 0.273 | 1.920 |
| **PSD1** | 5.331 | 1.666 | 3.498 | 1.832 | −3.498 | 3.339 | 0.272 | 1.909 |
| **PSD2** | 5.100 | 1.553 | 3.326 | 1.773 | −3.326 | 3.119 | 0.281 | 1.875 |
| **PSD3** | 5.029 | 1.513 | 3.271 | 1.758 | −3.271 | 3.043 | 0.284 | 1.860 |
| **PSD4** | 5.127 | 2.014 | 3.570 | 1.556 | −3.570 | 4.095 | 0.321 | 2.294 |
| **PSD5** | 5.349 | 1.685 | 3.517 | 1.832 | −3.517 | 3.375 | 0.272 | 1.919 |
| **PSD6** | 4.901 | 1.621 | 3.261 | 1.640 | −3.261 | 3.242 | 0.305 | 1.988 |
| **PSD7** | 5.311 | 1.633 | 3.472 | 1.839 | −3.472 | 3.277 | 0.271 | 1.887 |

[a] Units in eV. Softness in eV$^{-1}$.

**PSD6** ($-3.261$ eV). Likewise, chemical softness and hardness enumerate the extent of reactivity behavior and are inversely connected with each other. Compound depicted a larger energy gap is thought to have more hardness, stabile, and lest reactive.

On the other hand, a chromophore having reduced energy difference is considered as soft, displaying increased reactivity with reduced stability. All the studied compounds exhibited increased softness and reduced hardness values, thus being
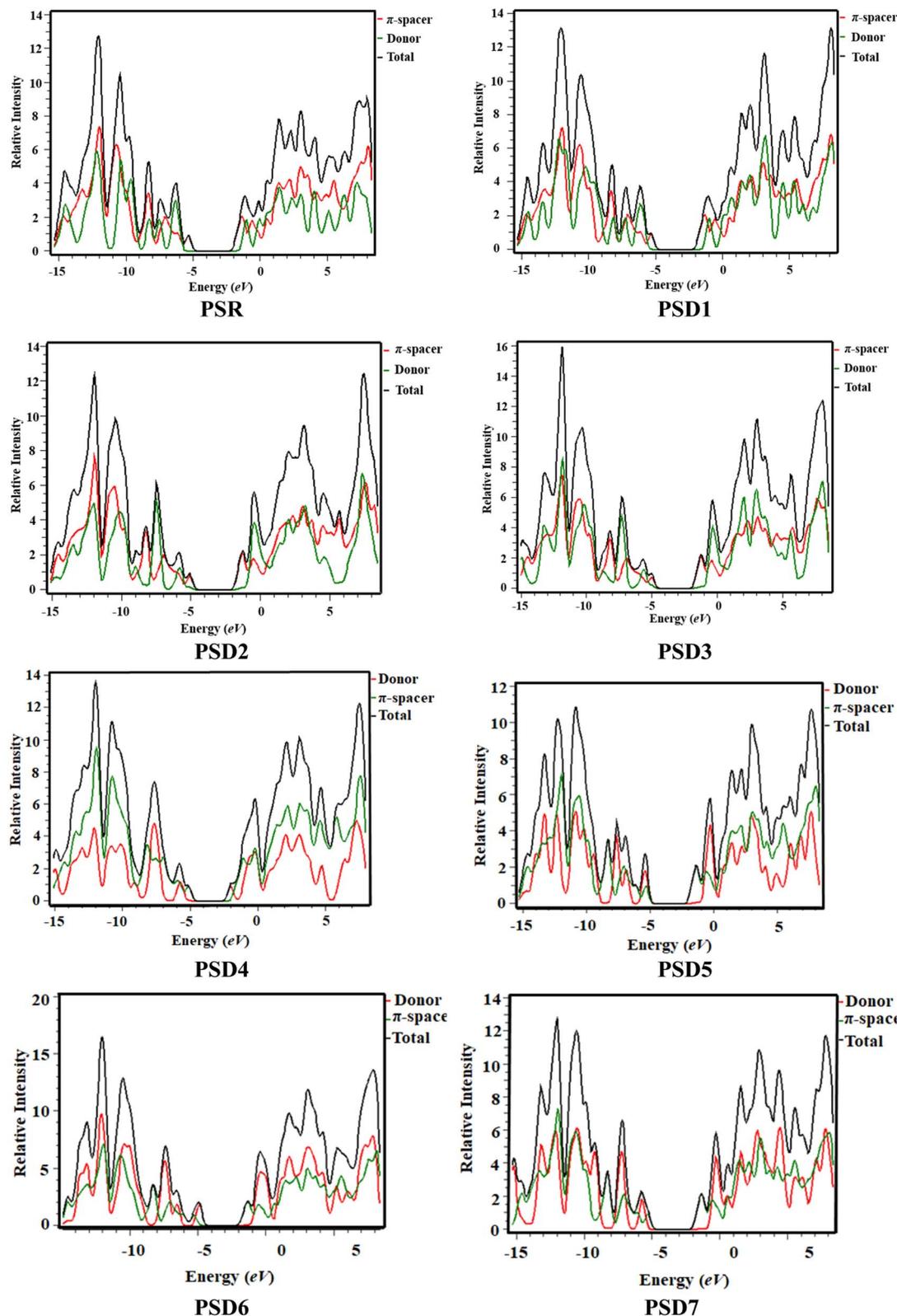


**Fig. 4** DOS plots of entitled compounds **PSR** and **PSD1–PSD7**.

considered electrically responsive and potentially possessing valuable photoelectric characteristics.

### Density of states (DOS)

The DOS indicates the possibility of accessible electronic energy states at a definite energy level. A higher density of state value indicates a larger quantity of unoccupied states in comparison to energy levels.[55] The DOS evaluation for **PSR** and **PSD1–PSD7** is carried out and graphical representations are shown in Fig. 4. In DOS graphs, the left side on the horizontal-axis represent the HOMO, and right side values denoted LUMO. The difference between these bands signifies the energy gap. To examine the ICT, **PSR** and **PSD1–PSD7** are segmented into two components: the central π-spacer, shown in red, and the terminal donor (D), represented in green. The black band signifies the total electronic contribution across the entire molecule.

Table 3 demonstrates that in **PSR**, the donor group contributes 1.3% to the HOMO and 1.8% to the LUMO. Here, the π-spacer is the primary contributor to the HOMO, accounting for 98.7%, whereas the LUMO is mostly impacted by the π-linker, with a contribution of 98.2%. For substances **PSD1–PSD7**, the HOMO is substantially influenced by the donor units, with contributions of 1.2%, 15.9%, 21.9%, 95.8%, 99.1%, 1.8% and 99.1%, respectively. The LUMO is predominantly attributed to the donor moieties, with contributions of 1.8%, 5.5%, 5.4%, 0.8%, 98.3%, 98.4% and 98.3%, respectively. Also, the π-spacer provides charge distribution configurations of 98.8%, 84.1%, 78.1%, 4.2%, 0.9%, 98.2%, and 0.9% charge towards HOMOs and 98.2%, 94.5%, 94.6%, 99.2%, 1.7%, 1.6%, and 1.7% charge towards LUMOs in all the studied compounds, respectively. The DOS plot reveals that in the cases of **PSD4**, **PSD5** and **PSD7**, donor atoms contribute significantly to the states near the HOMO, confirming that the frontier orbitals are localized over the donor moieties. This localization indicates that donor substitution alters the electronic density distribution, strengthening electronic coupling between different segments. From above discussion, it is obvious that the HOMOs of all the derived entities are found on the π-linker, whereas the LUMOs are greatly present on the donor groups (see Fig. 4). Altogether, DOS research indicates considerable charge flow from π-linker to donor moieties in all the examined compounds.

### UV-visible analysis

One of the most essential characteristics of HTMs is their transparency to visible light when an inverse cell is employed; specifically, they must not demonstrate absorption in the visible spectrum (400–700 nm).[20,56] UV-vis was used to get insights into the optical absorption wavelength ($\lambda_{max}$), transition energy ($E$), and oscillator strength ($f_{os}$) of compounds to comprehend their characteristics. As shown in Table 4, TD-DFT calculations were used to quantify the absorption spectra[49] (Fig. 5) of the reference and its derivatives (**PSR** and **PSD1–PSD7**) in chloroform solvent and gas state to determine how core and donor moieties affect spectral characteristics. The detailed transitions of **PSR** and **PSD1–PSD7** are reported in Tables S10–S25.

Table 4 demonstrates that the $\lambda_{max}$ values for the designed compounds (**PSR** and **PSD1–PSD7**) fall within the range from 422.0 to 441.8 nm in the gas phase. Moreover, it is noted that the computed $\lambda_{max}$ value for examined compounds is greater than that of the reference one (**PSR**), except for **PSD1**, **PSD5**, **PSD6**, and **PSD7**, which show a blue shift. The $\lambda_{max}$ for the proposed compounds follows a declining sequence as: **PSD3** (441.8) > **PSD2** (437.9) > **PSD4** (435.0) > **PSR** (422.3) > **PSD1** (422.2) > **PSD5** (422.0) > **PSD6** (421.7) > **PSD7** (420.5) in nm. Specifically, compound **PSD3** exhibits a $\lambda_{max}$ value of 441.8 nm with the associated energy and $f_{os}$ of 2.807 eV and 1.043 for two separate transitions, illustrating their respective strength and the vital transition of the HOMO/LUMO (95%). It is important to note that ligands may exert an influence on the $\lambda_{max}$. Of all the developed compounds, **PSD7** displays the minimum $\lambda_{max}$ value of 420.5 nm. The related perpendicular excitation, specifically H/L, contributes to approximately 93% of the total transition strength, along with an energy of 2.949 eV and a $f_{os}$ value of 0.816.

In the solvent (chloroform) phase, the compounds under investigation display greater $\lambda_{max}$ values than **PSR**, except **PSD1** and **PSD5–PSD7** show blue shift (see Table 4). The $\lambda_{max}$ of all eligible compounds is calculated to be within the range of

**Table 3** Percentages of the donor and π-spacer for LUMO and HOMO

| Compounds | LUMO | | HOMO | |
| --- | --- | --- | --- | --- |
| | π-Spacer | Donor | π-Spacer | Donor |
| **PSR** | 98.2 | 1.8 | 98.7 | 1.3 |
| **PSD1** | 98.2 | 1.8 | 98.8 | 1.2 |
| **PSD2** | 94.5 | 5.5 | 84.1 | 15.9 |
| **PSD3** | 94.6 | 5.4 | 78.1 | 21.9 |
| **PSD4** | 99.2 | 0.8 | 4.2 | 95.8 |
| **PSD5** | 1.7 | 98.3 | 0.9 | 99.1 |
| **PSD6** | 1.6 | 98.4 | 98.2 | 1.8 |
| **PSD7** | 1.7 | 98.3 | 0.9 | 99.1 |

**Table 4** Wavelength ($\lambda_{max}$), excitation energy ($E$) and oscillator strength ($f_{os}$) of the investigated compounds in gas and solvent

| Phase | System | TD-DFT $\lambda_{max}$ (nm) | $E$ (eV) | $f_{os}$ | MO contributions |
| --- | --- | --- | --- | --- | --- |
| Chloroform | **PSR** | 428.8 | 2.892 | 1.064 | H → L (97%) |
| | **PSD1** | 428.5 | 2.893 | 1.081 | H → L (97%) |
| | **PSD2** | 444.3 | 2.790 | 1.317 | H → L (97%) |
| | **PSD3** | 448.4 | 2.765 | 1.374 | H → L (96%) |
| | **PSD4** | 442.3 | 2.803 | 1.554 | H → L+1 (89%) |
| | **PSD5** | 428.3 | 2.895 | 1.035 | H → L (97%) |
| | **PSD6** | 427.5 | 2.900 | 1.092 | H−2 → L (97%) |
| | **PSD7** | 426.4 | 2.907 | 1.103 | H → L (97%) |
| Gas | **PSR** | 422.3 | 2.936 | 0.788 | H → L (94%) |
| | **PSD1** | 422.2 | 2.936 | 0.811 | H → L (94%) |
| | **PSD2** | 437.9 | 2.831 | 0.986 | H → L (94%) |
| | **PSD3** | 441.8 | 2.807 | 1.043 | H → L (95%) |
| | **PSD4** | 435.0 | 2.850 | 0.695 | H−2 → L (12%) |
| | **PSD5** | 422.0 | 2.938 | 0.762 | H−2 → L (93%) |
| | **PSD6** | 421.8 | 2.940 | 0.823 | H−2 → L (93%) |
| | **PSD7** | 420.5 | 2.949 | 0.816 | H → L (93%) |
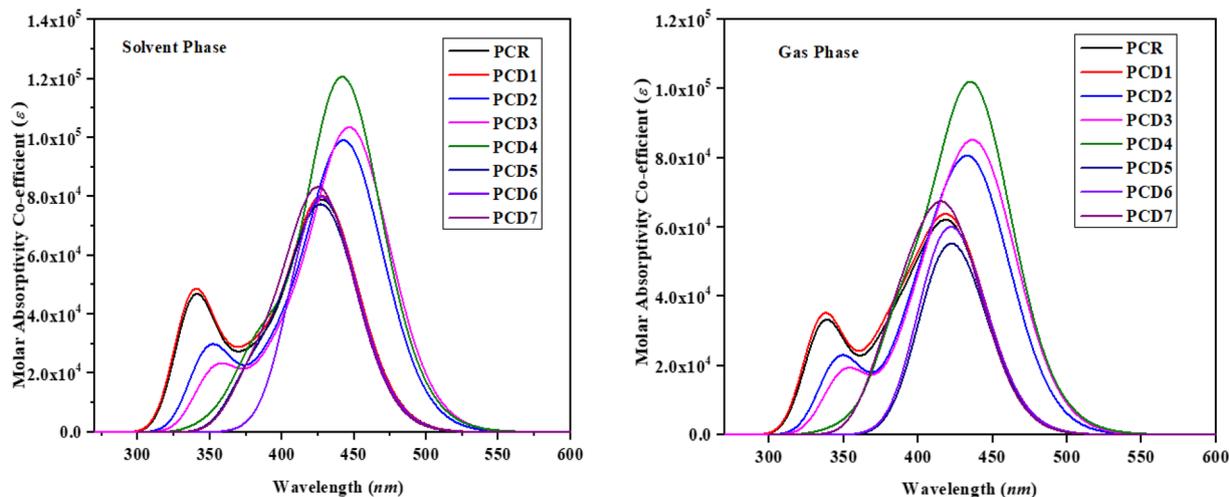
**Fig. 5** The computed absorption spectra of the studied substances PSR and PSD1–PSD7.

426.4–448.4 nm. **PSD3** exhibited the greatest $\lambda_{max}$ values of 448.4 nm with $f_{os}$ and $E$ values of 1.374 and 2.765 eV, respectively. The descending order of $\lambda_{max}$ of the entitled compounds is as follows: **PSD3** (448.4) > **PSD2** (444.3) > **PSD4** (442.3) > **PSR** (428.8) > **PSD1** (428.5) > **PSD5** (428.3) > **PSD6** (427.5) > **PSD7** (426.4 nm). Their associated energies (eV) are listed in the declining order as follows: **PSD7** (2.907) > **PSD6** (2.900) > **PSD5** (2.895) > **PSD1** (2.893) > **PSR** (2.892) > **PSD4** (2.803) > **PSD2** (2.790) > **PSD3** (2.765 eV). The observed increase in $\lambda_{max}$ and the decrease in excitation energy values suggest enhanced charge transfer capabilities within the chromophores, positioning them as promising options for HTMs. Among all, **PSD3** displays the largest $\lambda_{max}$ value in both gas and solvent phases, developing it into a proficient material exhibiting excellent photoelectronic characteristics in the area of HTMs. The red-shift in $\lambda_{max}$ originates from the reduced HOMO–LUMO gap and stronger $\pi$–$\pi^*$ transitions due to increased conjugation. The electron-donating strength enhances intramolecular charge transfer, thus lowering the excitation energy required for the transition.[57]

A comparison analysis of absorption spectrum with typical HTMs, such as spiro-OMeTAD,[20] shows significant agreement, indicating that the studied compounds are effective HTMs. Thus, the donor substitution introduces higher-energy $\pi$-orbitals that elevate the HOMO level, enhancing electronic delocalization across the $\pi$-system. This effect, evident in both FMOs and DOS analyses, reduces the HOMO–LUMO gap. The corresponding red-shift in UV-visible absorption confirms the improved intramolecular charge transfer arising from this orbital interaction in the investigated chromophores. These absorption wavelengths are comparable to or slightly blue-shifted relative to reported HTMs such as spiro-OMeTAD ($\lambda_{max}$ = 450–470 nm, $E_{exc}$ = 2.65–2.75 eV) and **TAPC** ($\lambda_{max}$ = 430–460 nm, $E_{exc}$ = 2.70 eV).[58,59] The relatively high oscillator strengths of the presented compounds indicate efficient $\pi$–$\pi^*$ transitions, confirming strong intramolecular charge transfer (ICT) similar to that in conventional HTMs. Hence, these derivatives can serve as promising HTM candidates with comparable or improved photo-absorption capabilities.

## Transition density matrix (TDM)

For assessing and understanding electronic excitation processes in molecular systems, the TDM is a powerful tool. Furthermore, it aids in analyzing relationships between donor and acceptor groups, electron and hole overlaps, and the degree of ICT.[60] All the developed chromophores (**PSR–PSD7**) are examined at initial excitation state ($S_1$) utilizing a similar basis set and level (Fig. 6). This investigation highlighted that the H-atoms are neglected owing to their minimal impact on CT. For the current analysis, compounds are divided into two different parts. This study generates a 3-D map with significant color variants, as illustrated with dark blue zone.

Maps of TDM indicated notable oblique flow of electric cloud from the center, to terminal moieties (D) in **PSR** and **PSD1–PSD7**. Except **PSD4** and **PSD6**, which is an exceptional case shows minimal charge is present only at donor region and not diagonally transfer as displayed in green and yellow spots over the dark blue backdrop. Also, the production of hole-electron pair and the flow of charges seemed to propagate in a non-diagonal way. These plots corroborated FMO and DOS results where an identical CT movement was observed.

## Exciton binding energy

In determining the molecular optoelectronic characteristics, the $E_b$ of electrons and holes (exciton) acts a critical role.[61] It indicates the energy necessary to discrete exciton pairs after the absorption of a photon, as it is closely related to the coulombic force. As $E_b$ decreases, coulombic interactions also diminish, leading to higher dissociation of exciton and enhanced transport of charge in the excited states. The $E_b$ for **PSR** and **PSD1–PSD7** is estimated *via* the eqn (8).

$$E_b = E_{H–L} - E_{opt} \qquad (8)$$

Here, $E_{H–L}$ denotes the LUMO/HOMO energy difference. $E_{opt}$ denotes the minimal energy necessary excitation from $S_0$ to the $S_1$.
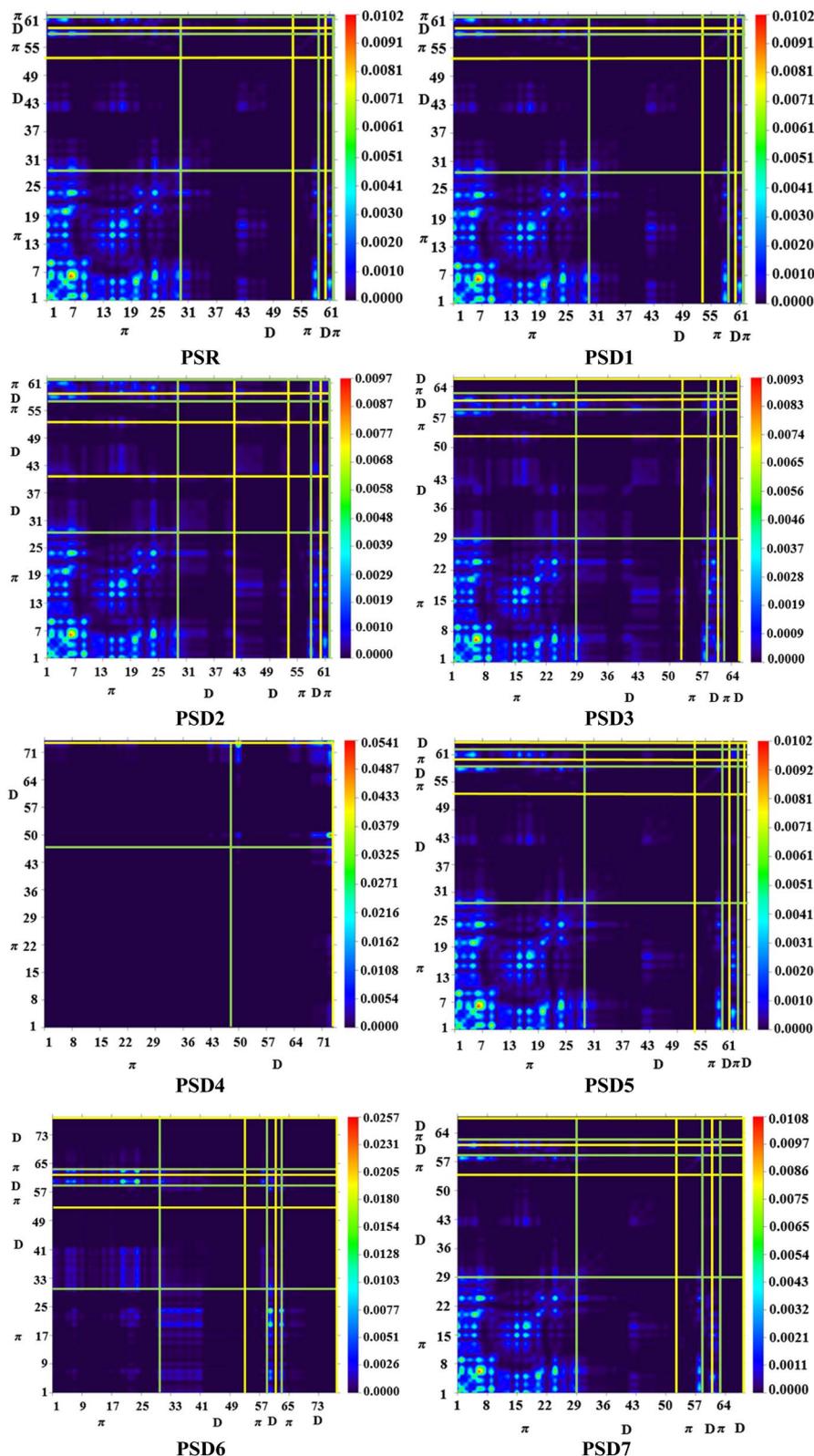
Fig. 6   TDM heat maps of **PSR** and **PSD1–PSD7** at initial excitation state.

Table 5 shows a comparable pattern to the $E_{H-L}$ found in $E_{opt}$. Moreover, the values of $E_b$ for **PSR** and **PSD1–PSD7** are determined to be 0.769, 0.772, 0.757, 0.751, 0.310, 0.769, 0.380, and 0.771 eV, correspondingly. **PSD4** had narrowest $E_b$ amidst all derivatives, representing its greater rate for the separation of excitons and potential to ominously improve the total current

**Table 5** Calculated $E_b$ of designed compounds (PSR and PSD1–PSD7)[a]

| Compounds | $E_{H-L}$ | $E_{opt}$ | $E_b$ |
|---|---|---|---|
| PSR | 3.661 | 2.892 | 0.769 |
| PSD1 | 3.665 | 2.893 | 0.772 |
| PSD2 | 3.547 | 2.790 | 0.757 |
| PSD3 | 3.516 | 2.765 | 0.751 |
| PSD4 | 3.113 | 2.803 | 0.310 |
| PSD5 | 3.664 | 2.895 | 0.769 |
| PSD6 | 3.280 | 2.900 | 0.380 |
| PSD7 | 3.678 | 2.907 | 0.771 |

[a] Units in eV.

density. The $E_b$ of studied substances drop as: **PSD1** > **PSD7** > **PSR**, **PSD5** > **PSD2** > **PSD3** > **PSD6** > **PSD4**. This reduced exciton binding energy ($E_b$) values demonstrate the stronger electron–hole pair dissociation associated with greater ICT.

### Hole–electron analysis

Analyzing hole electrons offers valuable insights into the efficacy of charge transporters and excitations within photovoltaic materials (**PSR** and **PSD1–PSD7**).[62] This analysis was performed with Multiwfn 3.8. This integrated technique confirms findings through frontier molecular orbital (FMO) and density of states (DOS) investigations, providing comprehensive insights into charge transfer and elucidating the characteristics of material optimization.[63]

According to Fig. 7, it was noticed that hole intensity is found high at numerous atoms of the π-linker part, expect **PSD4–PSD6**, as in the donor part, whereas intensity of electron is shifted at the donor region and found profound over the π-spacer, resulting in excellent ICT in all designed derivatives (**PSD1–PSD7**). Overall, the examined derivatives, **PSD1–PSD7**, including the reference compound, appeared to be electron-type materials, the findings indicate that electron intensity is significantly higher at the electronic band compared to the hole

intensity observed at the hole band (Fig. 7). Only the chemical **PSD4** is identified with an intensity ratio greater at the electronic band.

### Natural bonding orbital (NBO)

NBO analysis is a widely employed method for calculating natural charges in D–π–D-based compounds. It is highly effective for interpreting conjugative interactions and charge transfer processes within the system under study. Additionally, NBO analysis provides valuable insights into both inter- and intramolecular hydrogen bonding.[64] Furthermore, this approach is crucial for understanding the accurate representation of charge distribution density transfer from bonding, occupied, or Lewis-type NBOs to non-bonded, unoccupied, or non-Lewis NBOs. By using the 2nd-order perturbation theory, we may examine the stabilization energy of compounds, and eqn (9) is applied for this purpose.[65]

$$E^2 = q_i \frac{\left(F_{i,j}\right)^2}{\varepsilon_j - \varepsilon_i} \tag{9}$$

$E^2$ indicated as energy of stabilization, is controlled by different parameters affecting donors and acceptors, given by subscripts i and j. In this context, $E_i$, $E_j$, $F_{i,j}$, and $q_i$ relate to particular components, including diagonal and off-diagonal elements of the NBO Fock matrix as well as the occupancy of orbitals.

Owing to overlapping of orbital, there are frequently four primary forms of electronic transitions in the examined compounds, including $\pi \to \pi^*$, $\sigma \to \sigma^*$, LP $\to \pi^*$, and LP $\to \sigma^*$. Out of all transitions, $\pi \to \pi^*$ is regarded as the most evident, whereas $\sigma \to \sigma^*$ is less clear. As stated by obtained data in Tables S26–S33, valuable extended conjugation among **PSR** and **PSD1–PSD7** are noticed to be present for the majority of possible and constant $\pi \to \pi^*$ transitions, i.e., $\pi$ (C11–C24) $\to$ $\pi^*$(C22–C25), $\pi$(C9–C27) $\to$ $\pi^*$(C29–C32), $\pi$(C63–C66) $\to$ $\pi^*$(C71–C77), $\pi$(C51–C57) $\to$ $\pi^*$(C47–C53), $\pi$(C22–C25) $\to$
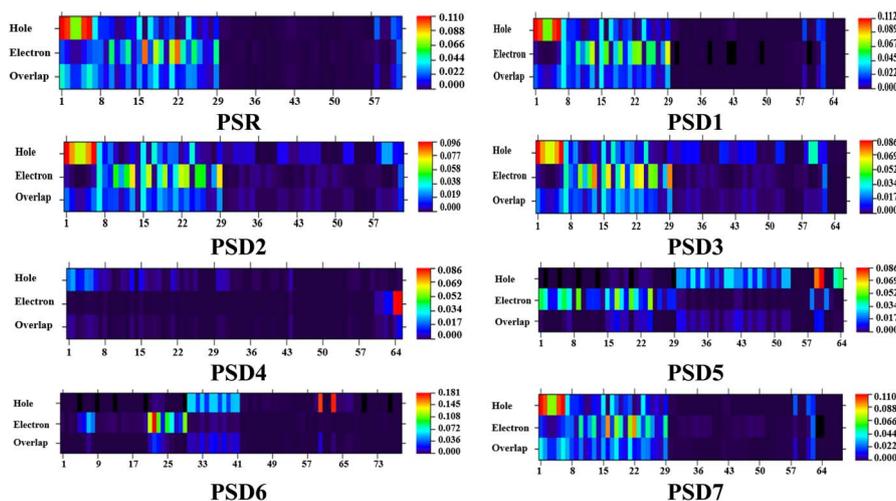


**Fig. 7** Hole electron analysis of PSR and PSD1–PSD7.

π*(C20–C21), π(C11–C20) → π*(C21–C22), π(C120–C122) → π*(C115–C117) and π(C62–C64) → π*(C68–C74) have the uppermost transition energies such as 27.45, 22.88, 24.02, 23.16, 25.03, 22.92, 25.39 and 24.35 kcal mol$^{-1}$, respectively, as a result of greater interactions among the donors and π-spacers, correspondingly. Whereas, the minimum energy π → π* interactions are π(C62–C65) → π*(C62–C65), π(C42–C45) → π*(C42–C45), π(C62–C64) → π*(C21–C22), π(C42–C44) → π*(C29–C32), π(C116–C118) → π*(C76–C78), π(C12–C102) → π*(C11–C20), π(C12–C102) → π*(C11–C20) and π(C12–C102) → π*(C11–C20) obtained with the related lowest energy values, *i.e.* 0.72, 0.79, 0.78, 0.77, 0.57, 14.66, 14.62 and 14.6 kcal mol$^{-1}$, accordingly for mentioned compounds.

In σ → σ* transitions, the highest stabilization energies obtained are 10.32, 10.32, 10.32, 10.31, 10.32, 10.32, 10.31, and 10.32 kcal mol$^{-1}$ for σ(C5–C8) → σ*(C4–N101), σ(C5–C8) → σ*(C4–N101), σ(C5–C8) → σ*(C4–N97), σ(C5–C8) → σ*(C4–N59), σ(C5–C8) → σ*(C4–N59), σ(C5–C8) → σ*(C4–N101), σ(C5–C8) → σ*(C4–N101) and σ(C5–C8) → σ*(C4–N101) transitions for **PSR** and **PSD1–PSD7**, appropriately. However, the minimum transition energy values are attained to be 0.99, 0.54, 0.59, 0.93, 0.55, 0.56, 0.53, and 0.92 kcal mol$^{-1}$ for σ(C2–C3) → σ*(C1–N101), σ(C61–N95) → σ*(C21–C22), σ(C22–N99) → σ*(C63–C66), σ(C53–H59) → σ*(C53–C57), σ(C117–H120) → σ*(C117–C119), σ(C63–N99) → σ*(C22–C25), σ(C125–H129) → σ*(C108–C112) and σ(C15–H19) → σ*(C13–C15) transitions in the investigated molecules.

In case of LP → π* transitions, *i.e.*, LP 1(N100) → π*(C43–C46), LP1(N94) → π*(C5–C8), LP1(C32) → π*(C9–C29), LP1(C22) → π*(C20–C21), LP1(N59) → π*(C1–C2), LP1(N98) → π*(C5–C8), LP1(N98) → π*(C5–C8) and LP1(N98) → π*(C5–C8), indicate the highest stabilization energies such as 40.78, 38.37, 75.45, 75.52, 38.53, 38.37, 38.38 and 38.4 kcal mol$^{-1}$ for **PSR** and **PSD1–PSD7**, accordingly. The LP → σ* transitions LP1 (N99) → σ*(C21–C22), LP1 (N96) → σ*(C29–C32), LP1 (N99) → σ*(C62–C64), LP1 (N96) → σ*(C42–C44), LP1 (N81→ σ*(C66–C68), LP1 (O104) → σ*(C47–C53), LP1 (N100) → σ*(C29–C32) and LP1 (N100) → σ*(C30–C32) exhibit the lowest transition energy values, *i.e.*, 5.44, 5.48, 2.29, 2.43, 2.55, 0.69, 6.01 and 5.5 kcal mol$^{-1}$, respectively. The comprehensive analysis of NBOs in the compounds under investigation has demonstrated that the high intramolecular charge mobility rate and extended hyper-conjugation are both essential for stabilizing the investigated chromophores and enhancing the CT properties that are important for the HTMs.

## Conclusion

The DHPP core-based chromophores with a D–π–D architecture have been engineered through structural modification with various heterocyclic donors to develop effective HTMs. Different types of extended electron-donating groups have been introduced to tune the photovoltaic and optoelectronic properties of DHPP-based HTMs. The energy gaps (ΔE) are found to be in the range of 3.11–3.678 eV, with a significant red shift ranging from 420.4 to 444.3 nm and lower binding energies ($E_b$ = 0.310–0.772 eV). The results demonstrate an elevated exciton dissociation

rate and substantial charge transfer from the HOMO to LUMO, corroborated by FMO, TDM, and DOS studies. All results show that the proposed chromophores possess potential for usage as hole transport materials owing to their good optical characteristics. Among all designed derivatives, **PSD3** and **PSD4** exhibit unique characteristics, such as reduced energy gaps (3.516 eV and 3.113 eV, respectively) with bathochromic shifts of 441.7 and 435.0 nm in the gas phase and 448.4 and 442.2 nm in the solvent phase, respectively. Furthermore, electron–hole analysis has been performed, identifying **PSD4** as the optimal chemical for the greatest electron–hole generation. The characteristics of **PSD4** with **TPA** donors enhance hole mobility and charge transfer, indicating that it is a good candidate for HTMs. Overall, the comparative analysis reveals that the designed DHPP core-based compounds exhibit electrical and optical characteristics, such as HOMO/LUMO energies, excitation energies, absorption wavelengths, and oscillator strengths, comparable to or even superior to those of conventional HTMs like spiro-OMeTAD and TAPC, highlighting their strong potential as efficient hole-transport materials for next-generation perovskite solar cells.

## Conflicts of interest

There is no conflict of interest to declare.

## Data availability

All data generated or analyzed during this study are included in the published article and its supplementary information (SI). Supplementary information is available. See DOI: **https://doi.org/10.1039/d5ra05824d**.

## Acknowledgements

## References

1  Z. Wang, Z. Li, J. Liu, J. Mei, K. Li, Y. Li and Q. Peng, *ACS Appl. Mater. Interfaces*, 2016, **8**, 11639–11648.

2  Q. Yue, W. Liu and X. Zhu, *J. Am. Chem. Soc.*, 2020, **142**, 11613–11628.

3  S. Ahmad, R. M. Tahar, F. Muhammad-Sukki, A. B. Munir and R. A. Rahim, *Energy*, 2015, **84**, 808–815.

4  A. Ndiaye, A. Charki, A. Kobi, C. M. Kébé, P. A. Ndiaye and V. Sambou, *Sol. Energy*, 2013, **96**, 140–151.

5  M. Abd Mutalib, F. Aziz, A. F. Ismail, W. N. W. Salleh, N. Yusof, J. Jaafar, T. Soga, M. Z. Sahdan and N. A. Ludin, *Appl. Mater. Today*, 2018, **13**, 69–82.

6  G. Xing, N. Mathews, S. Sun, S. S. Lim, Y. M. Lam, M. Grätzel, S. Mhaisalkar and T. C. Sum, *Science*, 2013, **342**, 344–347.

7 W. S. Yang, B.-W. Park, E. H. Jung, N. J. Jeon, Y. C. Kim, D. U. Lee, S. S. Shin, J. Seo, E. K. Kim and J. H. Noh, *Science*, 2017, **356**, 1376–1379.

8 Y. Rong, Y. Hu, A. Mei, H. Tan, M. I. Saidaminov, S. I. Seok, M. D. McGehee, E. H. Sargent and H. Han, *Science*, 2018, **361**, eaat8235.

9 J. Zhang, H. Lu, Y. Xu, C. Zhong, K. Chen, R. Tang, P. Zhang, F. Wu, R. He and L. Zhu, *J. Mater. Chem. C*, 2022, **10**, 14668–14674.

10 W. Sun, X. Zhao, E. Webb, G. Xu, W. Zhang and Y. Wang, *J. Mater. Chem. A*, 2023, **11**, 2092–2127.

11 H. D. Pham, L. Xianqiang, W. Li, S. Manzhos, A. K. K. Kyaw and P. Sonar, *Energy Environ. Sci.*, 2019, **12**, 1177–1209.

12 E. Sheibani, L. Yang and J. Zhang, *Sol. RRL*, 2020, **4**, 2000461.

13 Y. Zhu, G. Chen, Y. Zhong, W. Zhou, M. Liu and Z. Shao, *Mater. Today Energy*, 2017, **6**, 230–237.

14 L. Calió, S. Kazim, M. Grätzel and S. Ahmad, *Angew. Chem., Int. Ed.*, 2016, **55**, 14522–14545.

15 H. Wu, Y. Wang, X. Qiao, D. Wang, X. Yang and H. Li, *Chem. Mater.*, 2018, **30**, 6992–6997.

16 M. Tasior, O. Vakuliuk, D. Koga, B. Koszarna, K. Gorski, M. Grzybowski, Ł. Kielesiński, M. Krzeszewski and D. T. Gryko, *J. Org. Chem.*, 2020, **85**, 13529–13543.

17 G. Y. Erdemir, I. Knysh, K. Skonieczny, D. Jacquemin and D. T. Gryko, *J. Org. Chem.*, 2024, **89**, 15513–15522.

18 A. Janiga, E. Glodkowska-Mrowka, T. Stoklosa and D. T. Gryko, *Asian J. Org. Chem.*, 2013, **2**, 411–415.

19 M. Khalid, S. Jamal, A. A. C. Braga, M. Haroon, R. Alotaibi and K. Chen, *J. Saudi Chem. Soc.*, 2024, **28**, 101903.

20 I. Shafiq, M. Khalid, R. Jawaria, Z. Shafiq, S. Murtaza and A. A. Braga, *RSC Adv.*, 2024, **14**, 33048–33060.

21 W. T. Van Gompel, R. Herckens, P.-H. Denis, M. Mertens, M. C. Gélvez-Rueda, K. Van Hecke, B. Ruttens, J. D'Haen, F. C. Grozema and L. Lutsen, *J. Mater. Chem. C*, 2020, **8**, 7181–7188.

22 M. Krzeszewski, B. Thorsted, J. Brewer and D. T. Gryko, *J. Org. Chem.*, 2014, **79**, 3119–3128.

23 V. G. More, R. W. Jadhav, M. Al Kobaisi, L. A. Jones and S. V. Bhosale, *Handbook of Aggregation-Induced Emission*, 2022, pp. 221–253.

24 M. Frisch, F. Clemente, G. Scalmani, V. Barone, B. Mennucci, G. A. Petersson, H. Nakatsuji, M. Caricato, X. Li, H. P. Hratchian, A. F. Izmaylov, J. Bloino and G. Zhe, *Gaussian, 9*.

25 N. M. O'boyle, A. L. Tenderholt and K. M. Langner, *J. Comput. Chem.*, 2008, **29**, 839–845.

26 K. J. Stevenson, *J. Am. Chem. Soc.*, 2011, **133**, 5621.

27 T. Lu and F. Chen, *J. Comput. Chem.*, 2012, **33**, 580–592.

28 M. D. Hanwell, D. E. Curtis, D. C. Lonie, T. Vandermeersch, E. Zurek and G. R. Hutchison, *J. Cheminf.*, 2012, **4**, 1–17.

29 N. Swarnalatha, S. Gunasekaran, M. Nagarajan, S. Srinivasan, G. Sankari and G. Ramkumaar, *Spectrochim. Acta, Part A*, 2015, **136**, 567–578.

30 D. Pant, N. Darla and S. Sitha, *Comput. Theor. Chem.*, 2022, **1207**, 113522.

31 K. Fukui, *Science*, 1982, **218**, 747–754.

32 R. G. Parr, R. A. Donnelly, M. Levy and W. E. Palke, *J. Chem. Phys.*, 1978, **68**, 3801–3807.

33 D. G. Truhlar and P. Politzer, *Chemical Applications of Atomic and Molecular Electrostatic Potentials: Reactivity, Structure, Scattering, and Energetics of Organic, Inorganic, and Biological Systems*, Plenum Press, 1981.

34 R. Parthasarathi, J. Padmanabhan, M. Elango, V. Subramanian and P. Chattaraj, *Chem. Phys. Lett.*, 2004, **394**, 225–230.

35 R. G. Parr and R. G. Pearson, *J. Am. Chem. Soc.*, 1983, **105**, 7512–7516.

36 G. Sanil, B. Koszarna, Y. M. Poronik, O. Vakuliuk, B. Szymański, D. Kusy and D. T. Gryko, *Adv. Heterocycl. Chem.*, 2022, **138**, 335–409.

37 J. Pei, B. Gao, B. Li and Q. Duan, *New J. Chem.*, 2021, **45**, 3454–3462.

38 M. Wielopolski, J.-H. Kim, Y.-S. Jung, Y.-J. Yu, K.-Y. Kay, T. W. Holcombe, S. M. Zakeeruddin, M. Grätzel and J.-E. Moser, *J. Phys. Chem. C*, 2013, **117**, 13805–13815.

39 M. Khalid, L. Amir, M. Arshad, A. A. C. Braga and K. A. Alrashidi, *RSC Adv.*, 2025, **15**, 5965–5976.

40 M. R. S. A. Janjua, M. U. Khan, B. Bashir, M. A. Iqbal, Y. Song, S. A. R. Naqvi and Z. A. Khan, *Comput. Theor. Chem.*, 2012, **994**, 34–40.

41 M. R. S. A. Janjua, M. Amin, M. Ali, B. Bashir, M. U. Khan, M. A. Iqbal, W. Guan, L. Yan and Z. M. Su, *Eur. J. Inorg. Chem.*, 2012, 705–711.

42 M. Khan, M. Zafar, Z. Ullah, I. Shafiq, S. Bullo, T. Ahamad and K. Chen, *Sci. Rep.*, 2025, **15**, 26368.

43 M. I. Nan, E. Lakatos, G.-I. Giurgi, L. Szolga, R. Po, A. Terec, S. Jungsuttiwong, I. Grosu and J. Roncali, *Dyes Pigm.*, 2020, **181**, 108527.

44 W. Rahmalia, J.-F. Fabre, T. Usman and Z. Mouloungui, *Spectrochim. Acta, Part A*, 2014, **131**, 455–460.

45 M. Khan, M. Khalid, S. Murtaza, A. A. C. Braga, K. A. Alrashidi and S. Ahmed, *Sci. Rep.*, 2024, **14**, 19820.

46 M. U. Khan, M. Khalid, S. Asim, Momina, R. Hussain, K. Mahmood, J. Iqbal, M. N. Akhtar, A. Hussain and M. Imran, *Front. Mater.*, 2021, **8**, 719971.

47 M. Saliba, T. Matsui, J.-Y. Seo, K. Domanski, J.-P. Correa-Baena, M. K. Nazeeruddin, S. M. Zakeeruddin, W. Tress, A. Abate and A. Hagfeldt, *Energy Environ. Sci.*, 2016, **9**, 1989–1997.

48 A. Abate, T. Leijtens, S. Pathak, J. Teuscher, R. Avolio, M. E. Errico, J. Kirkpatrik, J. M. Ball, P. Docampo and I. McPherson, *Phys. Chem. Chem. Phys.*, 2013, **15**, 2572–2579.

49 R. G. Parr, L. v. Szentpály and S. Liu, *J. Am. Chem. Soc.*, 1999, **121**, 1922–1924.

50 N. Kovačević and A. Kokalj, *Corros. Sci.*, 2011, **53**, 909–921.

51 N. Sheela, S. Muthu and S. Sampathkrishnan, *Spectrochim. Acta, Part A*, 2014, **120**, 237–251.

52 M. Khalid, H. M. Lodhi, M. U. Khan and M. Imran, *RSC Adv.*, 2021, **11**, 14237–14250.

53 T. Koopmans, *Physica*, 1933, **1**, 104–113.

54 R. Meenakshi, *J. Mol. Struct.*, 2017, **1127**, 694–707.

55 A. J. Morris, R. J. Nicholls, C. J. Pickard and J. R. Yates, *Comput. Phys. Commun.*, 2014, **185**, 1477–1485.

56 J. D. Quezada-Borja, L. M. Rodríguez-Valdez, J. P. Palomares-Báez, M. A. Chávez-Rojo, L.-L. Landeros-Martinez, M. C. Martínez-Ceniceros, G. Rojas-George, I. A. García-Montoya and N. A. Sánchez-Bojorge, *Front. Chem.*, 2022, **10**, 907556.

57 M. Khalid, M. Khan, I. Shafiq, K. Mahmood, M. N. Akhtar, J. Iqbal, M. K. Al-Sadoon, W. Zaman and A. A. C. Braga, *Heliyon*, 2023, **9**, e13033.

58 Y. Yang, M. T. Hoang, D. Yao, N. D. Pham, V. T. Tiong, X. Wang and H. Wang, *J. Mater. Chem. A*, 2020, **8**, 12723–12734.

59 X. Sallenave, M. Shasti, E. H. Anaraki, D. Volyniuk, J. V. Grazulevicius, S. M. Zakeeruddin, A. Mortezaali, M. Grätzel, A. Hagfeldt and G. Sini, *J. Mater. Chem. A*, 2020, **8**, 8527–8539.

60 A. Sharif, S. Jabeen, S. Iqbal and J. Iqbal, *Mater. Sci. Semicond. Process.*, 2021, **127**, 105689.

61 S. Kraner, G. Prampolini and G. Cuniberti, *J. Phys. Chem. C*, 2017, **121**, 17088–17095.

62 Z. Liu, T. Lu and Q. Chen, *Carbon*, 2020, **165**, 461–467.

63 J. Geethapriya, A. Shanthidevi, M. Arivazhagan, N. Elangovan and R. Thomas, *J. Indian Chem. Soc.*, 2022, **99**, 100418.

64 M. A. Mumit, T. K. Pal, M. A. Alam, M. A.-A.-A.-A. Islam, S. Paul and M. C. Sheikh, *J. Mol. Struct.*, 2020, **1220**, 128715.

65 F. Weinhold and C. R. Landis, *Valency and Bonding: a Natural Bond Orbital Donor-Acceptor Perspective*, Cambridge University Press, 2005.